tvst

Article

Retinal Differential Light Sensitivity Variation Across the Macula in Healthy Subjects: Importance of Cone Separation and Loci Eccentricity

Danuta M. Sampson[1,2,*], Danial Roshandel[1,*], Avenell L. Chew[1], Yufei Wang[3], Paul G. Stevenson[4], Matthew N. Cooper[4], Elaine Ong[1], Lawrence Wong[1], Jonathan La[1], David Alonso-Caneiro[1,5], Enid Chelva[6], Jane C. Khan[1,7], David D. Sampson[8], and Fred K. Chen[1,7]

[1] Centre for Ophthalmology and Visual Science (Incorporating Lions Eye Institute), The University of Western Australia, Nedlands, Western Australia, Australia
[2] Surrey Biophotonics, Centre for Vision, Speech and Signal Processing and School of Biosciences and Medicine, University of Surrey, Guildford, United Kingdom
[3] Computer Science Department, University of Wisconsin-Madison, Madison, WI, USA
[4] Telethon Kids Institute, The University of Western Australia, Perth, Western Australia, Australia
[5] Contact Lens and Visual Optics Laboratory, School of Optometry and Vision Science, Queensland University of Technology, Queensland, Australia
[6] Department of Medical Technology and Physics, Sir Charles Gairdner Hospital, Nedlands, Western Australia, Australia
[7] Department of Ophthalmology, Royal Perth Hospital, Perth, Western Australia, Australia
[8] Surrey Biophotonics, School of Physics and School of Biosciences and Medicine, University of Surrey, Guildford, UK

Correspondence: Fred K. Chen, Lions Eye Institute, 2 Verdun Street, Nedlands 6009, Western Australia, Australia.
e-mail: fredchen@lei.org.au

Received: November 3, 2020
Accepted: March 29, 2021
Published: May 11, 2021

Keywords: photoreceptors; adaptive optics retinal imaging; microperimetry; retinal structure-function structure; normative data

Citation: Sampson DM, Roshandel D, Chew AL, Wang Y, Stevenson PG, Cooper MN, Ong E, Wong L, La J, Alonso-Caneiro D, Chelva E, Khan JC, Sampson DD, Chen FK. Retinal differential light sensitivity variation across the macula in healthy subjects: Importance of cone separation and loci eccentricity. Transl Vis Sci Technol. 2021;10(6):16, https://doi.org/10.1167/tvst.10.6.16

Purpose: Microperimetry measures differential light sensitivity (DLS) at specific retinal locations. The aim of this study is to examine the variation in DLS across the macula and the contribution to this variation of cone distribution metrics and retinal eccentricity.

Methods: Forty healthy eyes of 40 subjects were examined by microperimetry (MAIA) and adaptive optics imaging (rtx1). Retinal DLS was measured using the grid patterns: foveal (2°–3°), macular (3°–7°), and meridional (2°–8° on horizontal and vertical meridians). Cone density (CD), distribution regularity, and intercone distance (ICD) were calculated at the respective test loci coordinates. Linear mixed-effects regression was used to examine the association between cone distribution metrics and loci eccentricity, and retinal DLS.

Results: An eccentricity-dependent reduction in DLS was observed on all MAIA grids, which was greatest at the foveal-parafoveal junction (2°–3°) (−0.58 dB per degree, 95% confidence interval [CI]; −0.91 to −0.24 dB, $P < 0.01$). Retinal DLS across the meridional grid changed significantly with each 1000 cells/deg^2 change in CD (0.85 dB, 95% CI; 0.10 to 1.61 dB, $P = 0.03$), but not with each arcmin change in ICD (1.36 dB, 95% CI; −2.93 to 0.20 dB, $P = 0.09$).

Conclusions: We demonstrate significant variation in DLS across the macula. Topographical change in cone separation is an important determinant of the variation in DLS at the foveal-parafoveal junction. We caution the extrapolation of changes in DLS measurements to cone distribution because the relationship between these variables is complex.

Translational Relevance: Cone density is an independent determinant of DLS in the foveal-parafoveal junction in healthy eyes.

Introduction

Differential light sensitivity (DLS) perimetry has been widely used for investigating retinal diseases at the levels of the retinal ganglion cells and the postganglionic cells of the central visual pathways.[1–6] Standard automated perimetry is the current preferred method for measurement of retinal DLS for evaluation and follow-up of glaucomatous optic neuropathy.[7] However, it is impossible to know precisely to where in the retina the test stimulus is projected during the perimetry examination if the patient has unstable or eccentric fixation. In recent years, fundus-controlled perimetry (microperimetry) has gained widespread acceptance, in both routine clinical care and clinical trials, for assessing macular diseases that predominantly affect preganglionic cell pathways, mainly at the level of the photoreceptor cells and retinal pigment epithelium.[8,9] In contrast to conventional perimetry, microperimetry devices can track the retina using fundus landmarks and rapidly realign the target of the test stimulus to the intended test locus so that the intended retinal loci are measured and they are marked on a fundus image at completion. Hence, microperimetry provides pointwise DLS values, which can be correlated with structural and morphological features in images from other modalities. Despite its availability for over ten years, the comprehensive adjusted normal datasets and probability analyses that are routinely provided for standard automated perimetry are still lacking in current microperimetry instruments.[10] Although previous studies have shown that the normal "hill of vision" (as measured by DLS) has a sharp peak close to the foveal center within the macula,[11,12] microperimetry outcomes are still reported under the assumption that normal macular DLS varies around the same mean across all test loci.[13] Although one study has examined the relationship between cone photoreceptor density and DLS measurements in the central macula, it has some methodological limitations that require further refinement.[14]

Supriya et al.[14] used microperimetry and adaptive optics (AO) flood illumination retinal imaging to investigate the relationship between retinal DLS and cone photoreceptor arrangement in emmetropic eyes of young healthy volunteers aged 20 to 40 years. They showed a nonlinear relationship between the cone density (CD) measures and retinal DLS at eight retinal loci at the foveal-perifoveal junction (approximately 2° to 3° of visual angle eccentricity from the fixation point) with each locus showing a unique profile. This finding requires further investigation because DLS is believed to be related to the number of midget retinal ganglion cell receptive fields in the illuminated area rather than to CD.[15] Furthermore, loci beyond 3° of eccentricity, with the greater convergence of photoreceptor-to-ganglion cell input, were not examined. In addition, CD may have been underestimated in that study given that the authors did not consider examination of averaging of overlapping AO images. In our experience, this is an important step to enhance the quality of the final AO image and improve cone segmentation. Because macular DLS has become a surrogate marker for photoreceptor cell loss, the relationship between DLS and CD and other metrics of cone arrangement in healthy maculae warrant further characterization.

We conducted a retrospective study to measure macular DLS and quantify cone mosaic architecture using various metrics at 147 coregistered retinal locations per individual from 2° to 9° of eccentricity in a healthy population. The association of age, axial length, spherical equivalent, cone separation, and locus eccentricity, with retinal DLS measures was also examined.

Methods

Study Design

All research procedures described in this work were conducted according to the tenets of the Declaration of Helsinki. The research protocol was approved by The University of Western Australia Human Research Committee for two prospective studies enrolling healthy subjects (RA/4/1/7226, RA/4/1/7457). The circle Hough transform cone segmentation software was developed under a separate protocol (RA/4/1/7662).

Subjects were eligible if they had a normal ocular examination, a best-corrected visual acuity of 80 letters or more on the Early Treatment Diabetic Retinopathy Study chart (equivalent to Snellen acuity 20/25 or better) and were able to give informed consent. Subjects with a history of any ocular disease or surgery, use of medications that may potentially affect retinal photoreceptors (e.g., tamoxifen, hydroxychloroquine, and antipsychotics), media opacity, or refractive errors of greater than −6.0 diopters (D) of myopia, +4.0 D of hyperopia, or magnitude of greater than 4.0 D of astigmatism, were excluded. Multimodal imaging with spectral-domain optical coherence tomography, widefield retinal photography and fundus autofluorescence imaging were also applied to exclude any subjects

with retinal, macular or optic nerve disease (as assessed by the lead investigator, retinal specialist, F.K.C.).

Clinical Examination

All participants underwent complete ophthalmic examination, including: ocular biometry (IOL Master; Carl Zeiss Meditec, Inc., Dublin, CA, USA), autorefraction (Ark1, Auto Ref/ Keratometer; Nidek, Gamagori, Japan), widefield retinal photography (Optos, Inc, Marlborough, MA, USA), spectral-domain optical coherence tomography, near-infrared reflectance (NIR), and fundus autofluorescence imaging (Spectralis; Heidelberg Engineering, Heidelberg, Germany) of the macular region (30° × 30°), microperimetry (Macular Integrity Assessment, MAIA; Centervue, Padova, Italy) and AO flood illumination ophthalmoscopy (AO-FIO, rtx1; Imagine Eyes, Orsay, France) in the healthy eye (if both eyes were healthy, one was chosen at random). All measurements were performed by trained operators.

Microperimetry

Microperimetry is a fundus-controlled form of perimetry that combines fundus imaging, real-time tracking, and retinal DLS mapping. The retinal fundus image is captured by an infrared scanning laser ophthalmoscope. Retinal DLS is defined as the minimum light intensity that a patient can perceive when the test stimulus is projected onto the retina. The test grid arrangement can be customized by varying the number of, and separation between, stimuli within the central 20° of visual field. In both prospective studies (RA/4/1/7226, RA/4/1/7457), two types of grid patterns (A & B) were used. A third grid pattern (C) was also used in one of these two studies (RA/4/1/7226). Grids A and B are standard protocols that are used routinely in clinical practice. Grid C was designed to test the meridional locations (which are not tested by Grid B) and cover extended locations with greater sampling density compared to Grid B (7 loci 6° vs. 3 loci 4°). Grids A, B, and C cover foveal (2°–3° eccentricity), macular (3°–7° eccentricity), and meridional (2°–8° on horizontal and vertical meridians) regions, respectively (Figs. 1D–1F).

For analysis, test loci in Grid A and B are grouped into five nested rings, with Grid A providing DLS measurements in the foveal-perifoveal junction (ring numbers 1 and 2) and Grid B, the parafoveal region (rings numbers 3 to 5). Grid C data were used for analysis of parameters along horizontal and vertical meridians. The specific retinal locations (MAIA test loci) grouped to form each ring are shown in Figures 1G and 1H (for more details, see Supplementary Fig. S1).

In the MAIA device, the light stimuli are created by a white light-emitting diode and projected directly onto the retinal surface, whilst fundus landmarks are tracked at 25 Hz. The stimuli size is Goldmann III, background luminance is 4 apostilbs (asb), and maximum luminance is 1000 asb, with a 36 dB dynamic range. The decibel scale used in MAIA is inverted relative to the conventional decibel definition, so that dB = 10 log (reference intensity/measured intensity), where the reference intensity is set to the maximum value, corresponding to 0 dB. As the intensity is reduced, the dB value increases; thus, 20 dB stimulus is 100 times smaller than the maximum 0 dB. It is then color-coded according to the MAIA normative studies: where green represents normal values (25 dB or above), yellow suspect (13–24 dB), red abnormal (0–12 dB), and black (below 0 dB) dense scotoma. To measure the minimum retinal DLS at each location, the Goldmann III stimulus (0.43° size) is projected onto the same spot repeatedly using a 4-2 staircase thresholding strategy. Patients are seated in a dark room for 10 minutes before commencing the test. They are given an opportunity to practice using the response trigger, and light scatter from the side was minimized by covering the computer screen with a red Perspex cover and patching of the contralateral eye. The room is completely darkened during the entire microperimetry testing session (MAIA manual).

Adaptive Optics Flood Illumination Ophthalmoscopy

The photoreceptor outer segment mosaic images were collected using AO-FIO under dim light conditions without dark adaptation as described in detail elsewhere.[16] Each AO image represents a 4° × 4° (750 × 750 pixels, which is further converted to 1500 × 1500 pixels) region in the retina. In linear dimensions, this equates to approximately 1.2 × 1.2 mm. The resolution of the system is 250 line-pairs per mm. This limits the ability to distinguish the very densely packed cones in close proximity to the fovea. Essentially, images obtained at retinal eccentricities within 2° from the foveal center are not reliable for performing cone metrics.[17]

The images were collected retrospectively from two prospective studies each with different acquisition protocols. In the first study (RA/4/1/7226), the image acquisition protocol specified collection of 20 single AO images with an overlap of 2° field of view. In the second study (RA/4/1/7457), 29 single

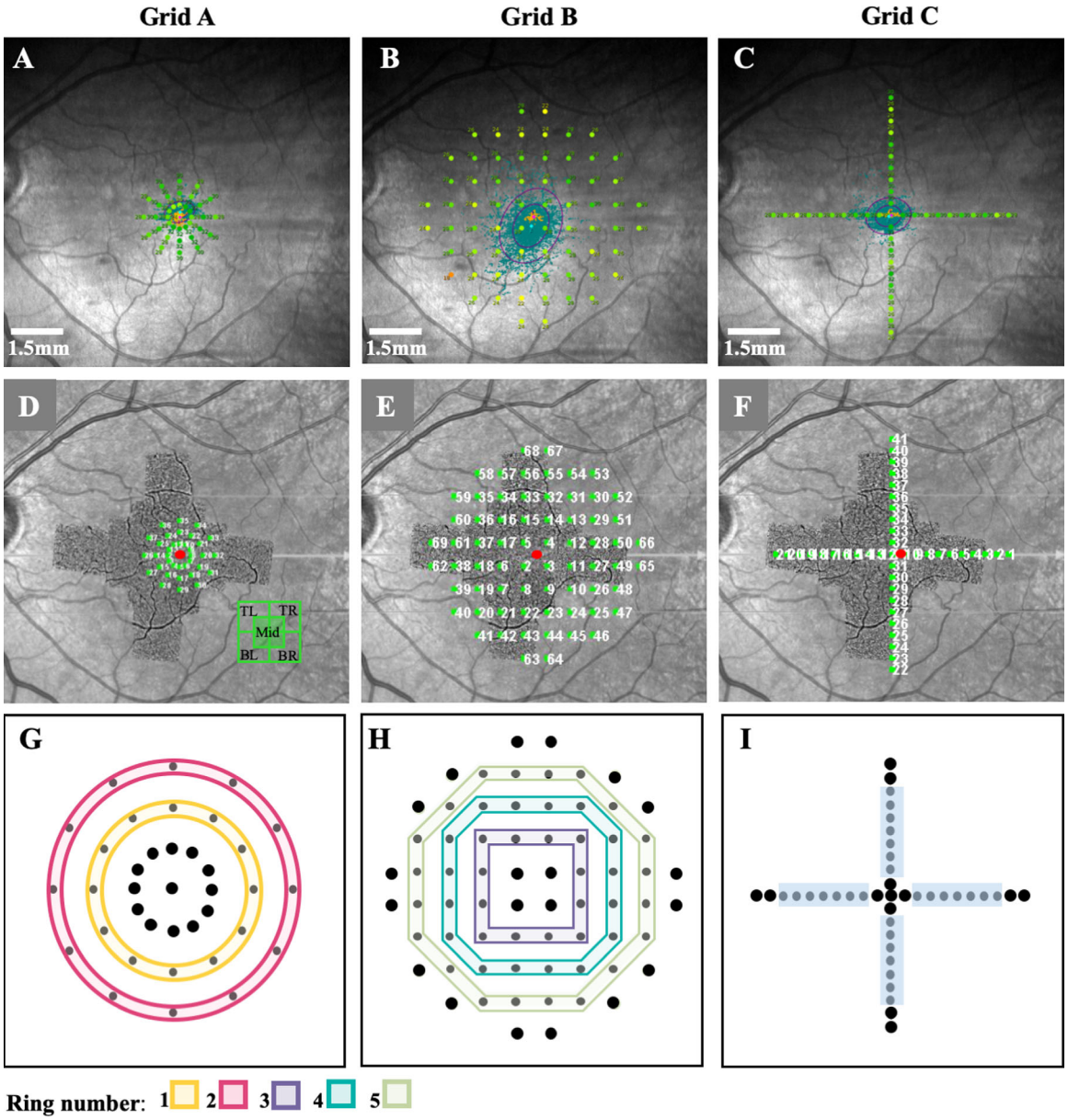

Figure 1. Fundus images showing the three MAIA testing grids used in this study (**A**–**C**). AO-FIO images were aligned and merged into a mosaic that can be overlaid (seen as darker region) on the MAIA fundus images using vascular landmarks for image registration. Note that the preferred retinal locus (*red dot*) is located temporal to the anatomical fovea in all grids (**D**–**F**). At each region of interest (*green dots*, corresponding to MAIA test loci), five sampling windows (TL, top left; TR, top right; BL, bottom left; BR, bottom right; Mid, middle) from the AO mosaic are extracted for quality assessment and cone counting. Test loci are grouped into five rings: ring numbers 1 and 2 are from Grid A, marked in *yellow* and *pink* (**G**), whereas ring numbers 3, 4, and 5 are from Grid B, marked in *purple*, *blue*, and *gray*, respectively (**H**). Horizontal and vertical loci 2° to 8° away from the fovea were also analyzed (**I**). Loci in *black* color are not used for analysis of cone distribution metrics. Ring 1 (2°), ring 2 (3°), ring 3 (3.2° & 4.2°), ring 4 (5.1° & 5.8°), and ring 5 (7.1° & 7.6°). *Scale bar*: 1.5 mm as shown in top row.

AO images with an overlap of 1° field of view were collected. These single AO images were used to create a widefield montage, as demonstrated in Figures 1D to 1F. Overlapping single AO images were stitched together using the MosaicJ plugin for ImageJ (Laboratory for Optical and Computational Instrumentation, Madison, WI, USA). Macular volumetric scans (61 horizontal B-scans each separated by approximately 130 µm) were used to determine and mark the center of the foveal dip aligned to the fovea externa on the accompanying high-resolution NIR image. The location of the foveal center in the widefield AO montage was determined through alignment with the NIR image with center marked using Adobe Photoshop CS6 (Adobe Systems, Inc., San Jose, CA, USA). To convert metric units to angular units and

Table 1. Demographic, Axial Length, Spherical Equivalent, and Fixation Data of Participants

						Grid A		Grid B		Grid C	
ID	Age (Year)	Sex	Eye	AXL (mm)	SE (D)	D1	D2	D1	D2	D1	D2
1	67	F	LE	24.53	−1.00	2.6	1.7	5.0	6.7	3.8	3.1
2	29	M	RE	23.40	−0.50	1.3	1.2	1.4	1.1	1.6	1.4
3	68	F	RE	23.12	1.75	2.4	2.1	9.1	5.8	6.1	3.7
4	65	M	LE	24.68	0.25	1.3	0.9	1.7	1.5	1.3	1.0
5	57	M	LE	23.99	0.25	1.3	1.3	1.6	1.2	1.6	1.2
6	32	M	LE	24.87	−3.50	1.7	1.3	1.9	1.5	2.6	2.1
7	58	M	RE	23.63	0.88	1.2	0.8	1.4	1.1	1.5	1.1
8	69	M	RE	25.59	−1.75	1.5	1.2	1.4	1.1	1.2	1.1
9	70	M	LE	22.69	2.75	1.0	0.7	0.8	0.8	1.1	1.0
10	70	F	RE	23.89	2.25	1.3	1.0	4.0	3.5	1.2	1.0
11	69	M	LE	24.25	−0.13	1.9	1.7	7.3	4.1	1.3	0.9
12	65	F	RE	23.09	2.00	1.6	1.1	1.5	1.4	1.0	0.8
13	75	M	RE	24.65	0.75	4.9	3.4	5.4	4.4	4.0	3.5
14	65	F	LE	23.24	1.88	1.5	1.4	4.6	2.6	1.5	1.3
15	22	M	RE	23.75	0.00	0.6	0.5	0.7	0.6	0.6	0.5
16	21	M	RE	25.40	−4.75	1.0	0.8	1.3	0.9	1.1	0.8
17	54	F	RE	24.80	0.50	1.7	1.3	2.4	2.1	1.8	1.2
18	68	M	LE	24.64	−0.25	1.5	1.0	1.3	1.0	1.6	1.4
19	49	M	LE	24.15	−0.25	1.4	1.0	7.3	1.8	1.7	0.5
20	52	M	RE	23.99	−0.13	3.0	2.2	7.6	4.2	3.5	1.6
21	54	F	RE	24.45	0.00	1.3	1.3	2.8	2.3	1.9	1.7
22	58	M	RE	23.99	−3.25	1.2	0.9	1.3	1.1	1.2	0.7
23	64	F	RE	23.08	−0.25	4.0	3.1	4.6	2.4	3.2	2.6
24	69	F	LE	22.65	0.50	1.9	1.4	2.7	2.3	2.5	2.2
25	44	M	RE	25.01	0.13	1.7	1.4	2.4	1.2	3.3	2.0
26	70	F	RE	22.56	1.00	1.6	1.6	3.2	2.1	2.2	1.7
27	62	F	RE	23.83	−1.38	1.4	1.1	3.7	2.7	2.2	1.4
28	62	F	RE	23.16	0.75	1.1	0.8	1.2	0.9	0.8	0.8
29	59	M	LE	23.69	−0.50	1.1	0.9	1.1	0.6	1.3	0.6
30	53	F	RE	23.95	1.25	1.1	1.0	2.2	1.7	1.3	1.2
31	25	F	RE	24.88	−3.25	2.1	1.6	4.1	3.1	1.9	1.8
32	57	F	RE	23.94	−0.50	NA	NA	4.7	2.6	NA	NA
33	68	M	LE	23.95	−0.63	NA	NA	5.1	2.9	NA	NA
34	53	M	RE	26.10	−4.50	NA	NA	2.3	1.7	NA	NA
35	44	M	LE	23.93	−0.50	NA	NA	1.8	1.4	NA	NA
36	64	M	RE	25.18	−3.75	NA	NA	1.8	1.3	NA	NA
37	45	F	RE	25.00	−5.00	NA	NA	1.6	1.3	NA	NA
38	64	M	LE	24.69	−3.63	NA	NA	1.8	1.7	NA	NA
39	55	F	LE	23.12	1.13	NA	NA	1.1	0.8	NA	NA
40	64	M	LE	24.03	−0.25	NA	NA	3.2	2.0	NA	NA

D1 and D2 are Bivariate Contour Ellipse Area 95% (BCEA 95%) long and short diameters in degrees.
AXL, axial length; D, diopters; LE, left eye; NA, not available; RE, right eye; SE, spherical equivalent.

align the AO montage with other image modalities, all AO images were corrected for magnification error related to axial length variation using the modified Littmann's method described by Bennett et al.,[18] as per the equation: $q = 0.013063 \times$ (axial length in mm − 1.82), where q is the magnification factor for that eye. Refer to Chew et al. [19] for more details.

Retinal regions of interest (ROI) were chosen to coincide with microperimetry test loci from the three testing grids. Each ROI was divided into five

Table 2. Number and Proportion of Analyzed AO Samples and Available AO and MAIA Data in Each Grid/Ring/Eccentricity

Grid	Ring	Distance (Degrees)	Total Samples	AO Data Available (%)	AO and MAIA Data Available (%)	DLS (dB)	CD (Cell/Deg^2)	ICD(Arcmin)
A	1	2.0	480	466 (97%)	359 (75%)	29.7 (2.4)	2209 (155)	1.5 (0.1)
	2	3.0	480	463 (96%)	358 (75%)	29.0 (2.2)	1857 (161)	1.6 (0.1)
	Total		960	929 (97%)	717 (75%)	29.4 (2.3)	2034 (236)	1.5 (0.1)
B	3	3.2 & 4.2	480	413 (86%)	413 (86%)	28.0 (2.2)	1809 (151)	1.6 (0.1)
	4	5.1 & 5.8	640	309 (48%)	281 (44%)	27.9 (2.2)	1731 (143)	1.6 (0.1)
	5	7.1 & 7.6	800	111 (14%)	111 (14%)	27.6 (2.1)	1534 (134)	1.8 (0.1)
	Total		1920	833 (43%)	805 (42%)	27.9 (2.2)	1743 (171)	1.6 (0.1)
C	2	2.0	160	153 (96%)	117 (73%)	29.3 (2.5)	2211 (167)	1.5 (0.1)
	3	3.0	160	150 (94%)	87 (54%)	29.0 (2.3)	1895 (173)	1.6 (0.1)
	4	4.0	160	144 (90%)	113 (71%)	28.4 (2.0)	1765 (145)	1.6 (0.1)
	5	5.0	160	131 (82%)	103 (64%)	28.3 (2.2)	1720 (146)	1.6 (0.1)
	6	6.0	160	104 (65%)	80 (50%)	28.4 (2.2)	1536 (137)	1.8 (0.1)
	7	7.0	160	85 (53%)	67 (42%)	27.3 (2.4)	1523 (135)	1.8 (0.1)
	8	8.0	160	51 (32%)	40 (25%)	26.8 (2.7)	1561 (170)	1.7 (0.1)
	Total		1120	818 (73%)	607 (54%)	28.4 (2.4)	1798 (281)	1.6 (0.1)
Total	—		4000	2580 (64%)	2129 (53%)	28.6 (2.4)	1865 (266)	1.6 (0.1)

overlapping sampling windows measuring 50 × 50 µm. These ROIs were extracted using automated custom software for the analysis of cone metrics. Further image-processing, namely, cone segmentation using a Hough transform and image quality assessment, were undertaken for each sampling window. The sampling window with the best image quality and highest number of cones was selected for further analysis. Loci with poor image quality (for example, truncated or with no visible cones) across all five overlapping sampling windows were excluded from further analysis.

Descriptive Metrics for Quantitative Assessment of Cone Photoreceptor Cell Architecture

A variety of metrics have been introduced to describe cone photoreceptor cell mosaics.[20] We used different cone regularity metrics, in addition to CD and ICD, to evaluate the correlation between retinal DLS and each parameter of the cone mosaic.[21–25] These include intercone distance (a measurement of cell-to-cell spacing using photoreceptor coordinates)[25–28] and regularity metrics, which assay the expected number of Voronoi sides for photoreceptor locations within a mosaic.[29-31]

Each cone distribution metric used in this study is expressed in either retinal linear units (e.g., linear distance in µm; area density in cells/mm^2) or visual angle units (e.g., angular distance in arc minutes; angular density in cells/deg^2).

For each sampling window, cone reflexes were first identified using the circle Hough transform segmentation method,[16] and their x and y coordinates were stored. Area and angular CD was then determined by dividing the total number of cells counted by the retinal area sampled in linear units (1000 cells/mm^2) or in angular units (1000 cells/deg^2).

To examine cone photoreceptor cell regularity, a Voronoi domain analysis was performed using the Matlab function, VoronoiLimit. The Voronoi cell boundaries were determined by finding the midpoints and vertices between neighboring cells in x and y coordinates, and from these boundaries the number of Voronoi neighbors and the sizes of each Voronoi cell were calculated. To diminish boundary effects, only cones with bound Voronoi regions were included when calculating each metric. The number of neighbors regularity is the ratio of the mean to standard deviation (SD) of the number of sides of all bound Voronoi cells in an ROI.[20] Linear and angular intercone distance (ICD) [µm and arcmin] was defined for each cone photoreceptor cell as the average distance between the cone and all of its neighbors; the value reported for each image is the average ICD for all cones with bound Voronoi cells in that image. Linear and angular farthest neighbor distance and nearest neighbor distance (NND) [µm and arcmin] were defined as the distance from a given cone photoreceptor cell to its

farthest and closest neighbor, respectively, where the neighbors comprised all cones with adjacent Voronoi cells. The values reported for each image are the average farthest neighbor distance and NND for all of the cones with bound Voronoi cells in that image.[20] NND was compared with the expected spacing of cell centers in a triangularly packed mosaic with the same cell density. The expected triangular spacing is calculated as $s = (\frac{2}{\sqrt{3}D})^{1/2}$, where s (µm or arcmin) is the spacing between the centers of triangularly packed cells and D (cells/µm^2 or cells/arcmin^2) is the cell density.[32] The nearest neighbor regularity index was calculated by dividing the mean nearest-neighbor distance by the standard deviation.[33]

Statistical Analysis

The Shapiro-Wilk test was used to test whether variables are normally distributed. Retinal DLS, ICD, and CD are represented with smoothed (kernel) density estimates (probability density function curves based on the histogram) and box plots. Linear mixed-effects models of retinal DLS by CD were built with the "nlme" package (Pinheiro, José, Douglas Bates, and R-core. 2018. Nlme: Linear and Nonlinear Mixed Effects Models. https://CRAN.R-project.org/package=nlme), with the patient ID as the random effect after adjusting for age and distance from the fovea. A Gaussian spatial correlation structure was employed. Patient sex, axial length and spherical equivalents were examined as covariates in the retinal DLS modeling.

Missing data were excluded from the analysis, and a P value = 0.05 was used as a threshold to guide the interpretation of observed associations. Basic analyses were performed in the Statistical Package for Social Sciences (SPSS, software version 24, IBM Corporation, Armonk, NY, USA), complex modeling of the relationship between CD and retinal DLS using linear mixed-effects regression analysis was performed in R v3.5.2 (R Core Team. 2018. R: A Language and Environment for Statistical Computing. Vienna, Austria: R Foundation for Statistical Computing. https://www.R-project.org/).

Results

Study Subjects

Forty eyes from 40 healthy subjects (31 from RA/4/1/7226 and nine from RA/4/1/7457) were enrolled for this study (17 female and 23 male). The mean (range) age of the participants was 56 (21–75) years (Table 1). The mean (SD; range) spherical equivalent refraction was −0.54 (1.98; −5.00 to 2.75) D. The mean (SD; range) axial length was 24.10 (0.84; 22.56 to 26.10) mm. The number and proportion of analyzed AO samples in each grid/ring/eccentricity is shown in Table 2. Figure 2 presents representative examples of both analyzed and excluded AO images at different rings. Individual data are presented as an Excel file in Supplementary Material S1.

Retinal Differential Light Sensitivity and Cone Distribution Metrics Across the Macula

The distribution of DLS at each eccentricity across the macula is shown in Figure 3. The smoothed density estimate graph shows an approximate normal distribution for each ring centered on 30 dB. However, there appears to be a relationship between increasing ring number (i.e., eccentricity) and decreasing DLS. Ring number 1, from Grid A, had the greatest mean DLS. The DLS declined as the ring diameter increased, i.e., as distance from the foveal center increased. This behavior is confirmed by the box plots in Figure 3 that show a decreasing median DLS over ring numbers 1 through 3 and an approximately stable median for ring numbers 4 and 5. The mixed-effects model shows no significant correlation between age or spherical equivalent and DLS (Supplementary Table S1).

Cone separation profile, reported as mean ICD (arcmin), taken at different diameter rings from Grids A and B, is illustrated in Figure 4. Ring number 1 has the lowest mean ICD, which increases with increasing diameter. The precision of these measurements also changes with diameter; the inner rings have a narrower distribution bandwidth; whereas, the density distributions of ring numbers 4 and 5 are broader. An inverse relationship between angular CD and ring number was observed, as illustrated in Figure 5, where ring number 1 has the highest density and as the ring number increases, the CD decreases. The mixed-effects model showed a statistically significant increase in CD (β estimate = 2 cells/deg^2/year, 95% confidence interval (CI); 0 to 3 cells/deg^2, P = 0.02) and decline in ICD (β estimate = $<$ −0.01 arcmin/year, 95% CI; $>$ −0.01 to $<$ 0.01 arcmin, P = 0.02) with increasing age, which was clinically negligible. In addition, there were no significant correlations between the spherical equivalent and CD or ICD (Supplementary Table S1).

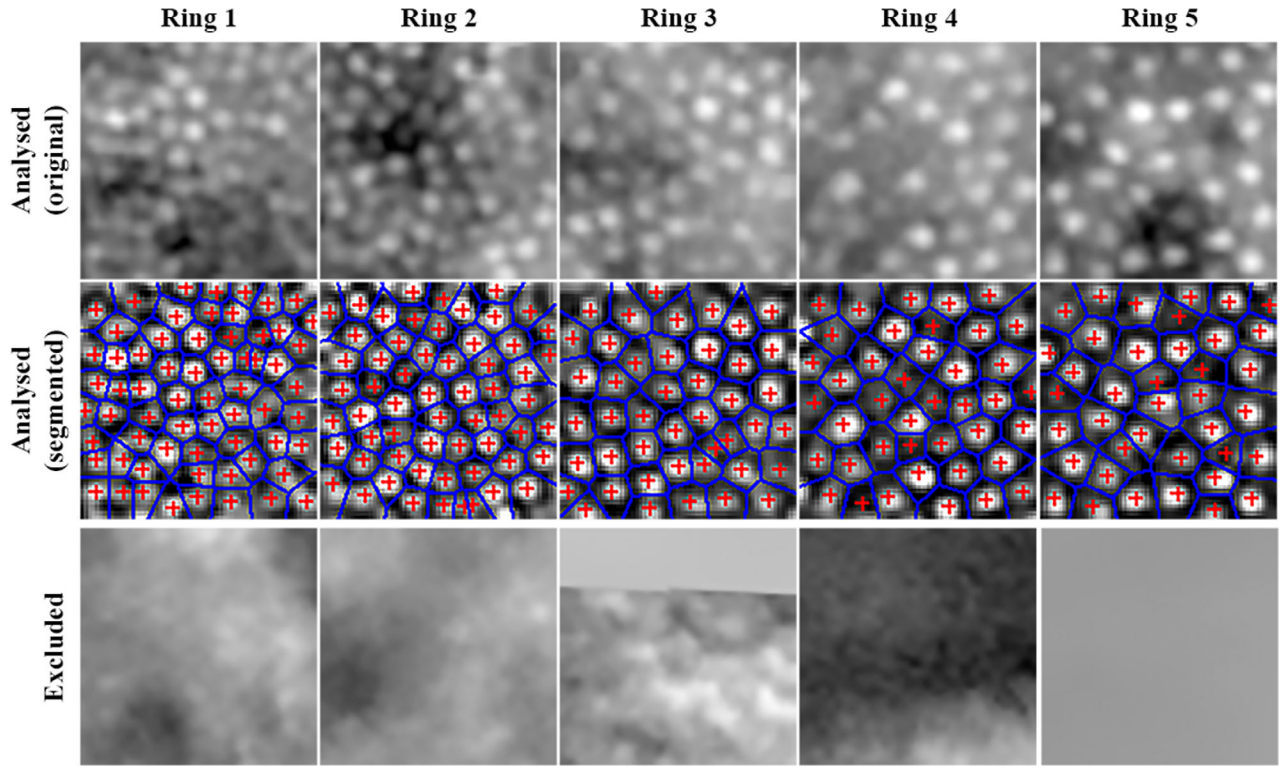

Figure 2. Representative examples of cone mosaic images included (*upper* and *middle row*) and excluded (*bottom row*) from the analysis. Reasons for exclusion are (from left to right): low image resolution, low image resolution, partial truncation, co-incidence with large vessel, and complete truncation.

Cone Distribution Metrics as Covariates for Differential Light Sensitivity at Foveal-Parafoveal Junction

Each of the cone distribution metrics was individually examined as a predictor for retinal DLS using a linear mixed-effects model after adjusting for patient age and angular distance from the fovea: $retinal\ DLS_i = \beta_1 \times cone\ metric_i + \beta_2 \times age_i + \beta_3 \times distance_i + \varepsilon_i$, where cone metric represents each of the metrics of cone distribution discussed earlier, in turn, and ε_i is the model's remaining random error; this was repeated for each of the three grid patterns and the results of the density estimators and 95% CIs are reported.

Cone density across Grid C was the only parameter with significant contribution to the retinal sensitivity (Table 3). Sensitivity changed by 0.85 dB for each 1000 cells/deg^2 change in CD across the Grid C (95% CI; 0.10 to 1.61 dB, $P = 0.03$) (Table 4). None of the other cone distribution parameters had a statistically significant effect on sensitivity on any of the grids. However, ICD showed a moderate to marked, but not significant correlation, with sensitivity across Grid A (β estimate = −0.74 dB, 95% CI; −2.42 to 0.95 dB, $P = 0.39$) and Grid C (β estimate = −1.36 dB, 95% CI; −2.93 to 0.20 dB, $P = 0.09$) (Table 5).

Angular Distance From Fovea as Covariate in Predicting Differential Light Sensitivity in Perifovea

When adjusting for the covariates age and angular CD, the angular distance from the fovea was found to have a negative association with DLS (Table 4); i.e., as the distance increased by 1°, the DLS decreased by 0.58 dB in Grid A (95% CI; −0.91 to −0.24 dB, $P < 0.01$); 0.12 dB in Grid B (95% CI; −0.22 to −0.02 dB, $P = 0.02$); and 0.23 dB in Grid C (95% CI; −0.35 to −0.11 dB, $P < 0.01$).

Discussion

We found a significant reduction in retinal DLS and CD, whilst ICD increased as the sampling locus moved further away from the foveal center. DLS had a

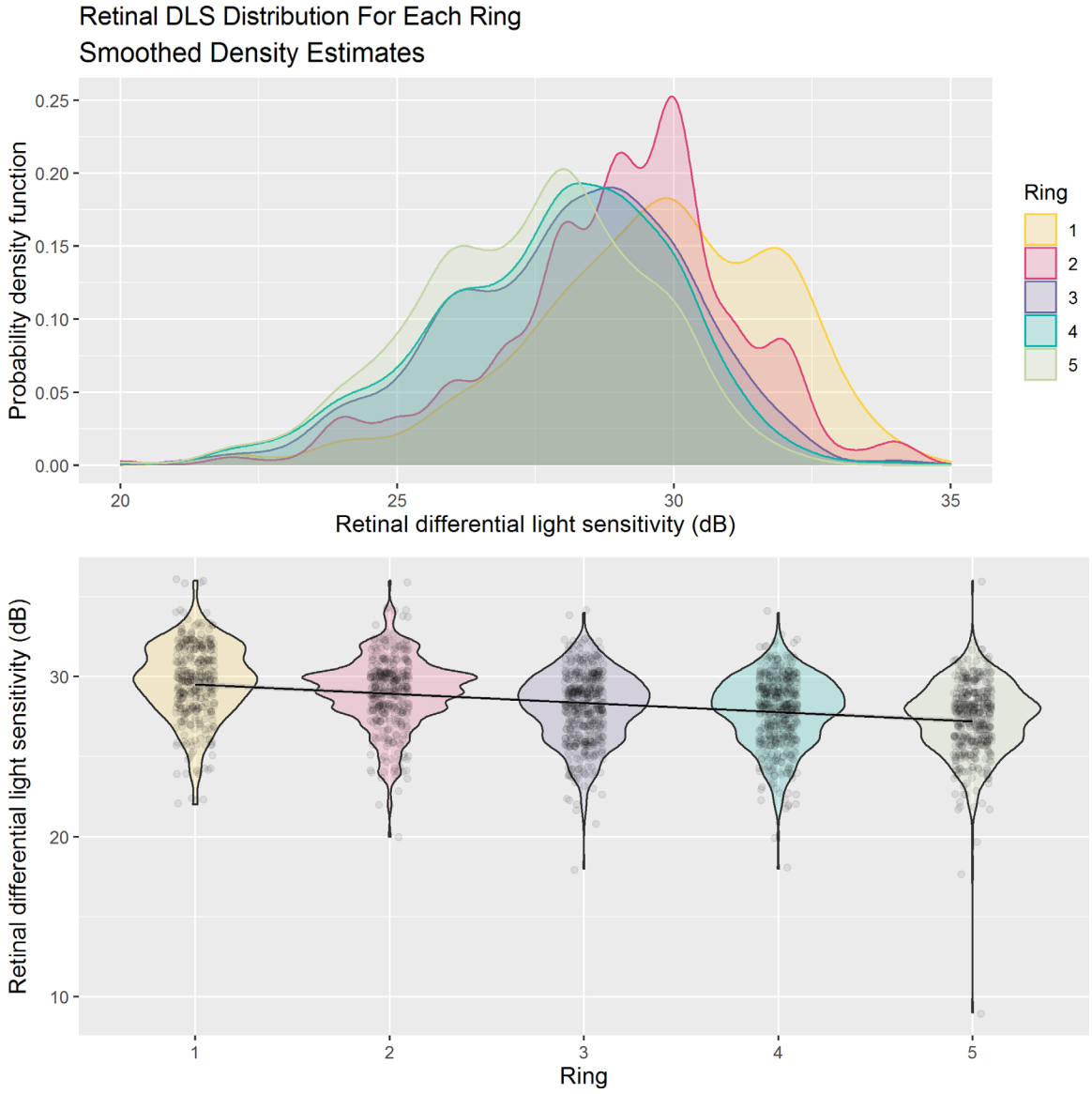

Figure 3. (*Top*) Five overlapping kernel density estimates (smoothed histogram) illustrate the shape of mean retinal DLS (dB) distribution in five groups of retinal loci from Grids A (ring numbers 1 and 2) and B (ring numbers 2, 3 and 4). (*Bottom*) A violin plot showing the mild trend for the mean retinal DLS to decrease as the ring number (diameter) increases (β estimate $= -0.48$ dB per ring number, 95% CI; -0.57 to -0.40 dB, $P < 0.01$). Ring 1 (2°), ring 2 (3°), ring 3 (3.2° and 4.2°), ring 4 (5.1° & 5.8°), and ring 5 (7.1° and 7.6°).

significant inverse correlation with cone density in the meridional test grid, but not in the parafoveal (2°–3°) and perifoveal (5°–7°) regions, where retinal eccentricity, but not cone packing, was correlated with DLS.

Topography of the retinal DLS in healthy people is likened to a "hill of vision" based on perimetry findings; however, the shape of this "hill" varies depending on factors such as stimulus size and duration.[34] Previous studies showed a slight decrease of DLS in the macular region with increasing retinal eccentricity in both microperimetry and Humphrey field tests, which is in agreement with our findings.[34–37] According to the MAIA pointwise sensitivity data, in 60 cases aged 19 to 50 years (mean 24 years, median 23 years) provided by Astle and colleagues,[13] mean DLS at 3°, 5°, 7°, and 9° were 30.1, 29.9, 29.4, and 29.0 dB, respectively. These sensitivity values are 2 to 3 dB higher than our observation at the same eccentricities, possibly because of the participants being older in our cohort (range 21–75, mean 56 years). In another study on a Japanese population (mean age 43 years), mean MAIA threshold at 3° and 5° locations were 28.7 and 27.8 dB, respectively, which are closer to our values.[35] The relatively shallow slope of

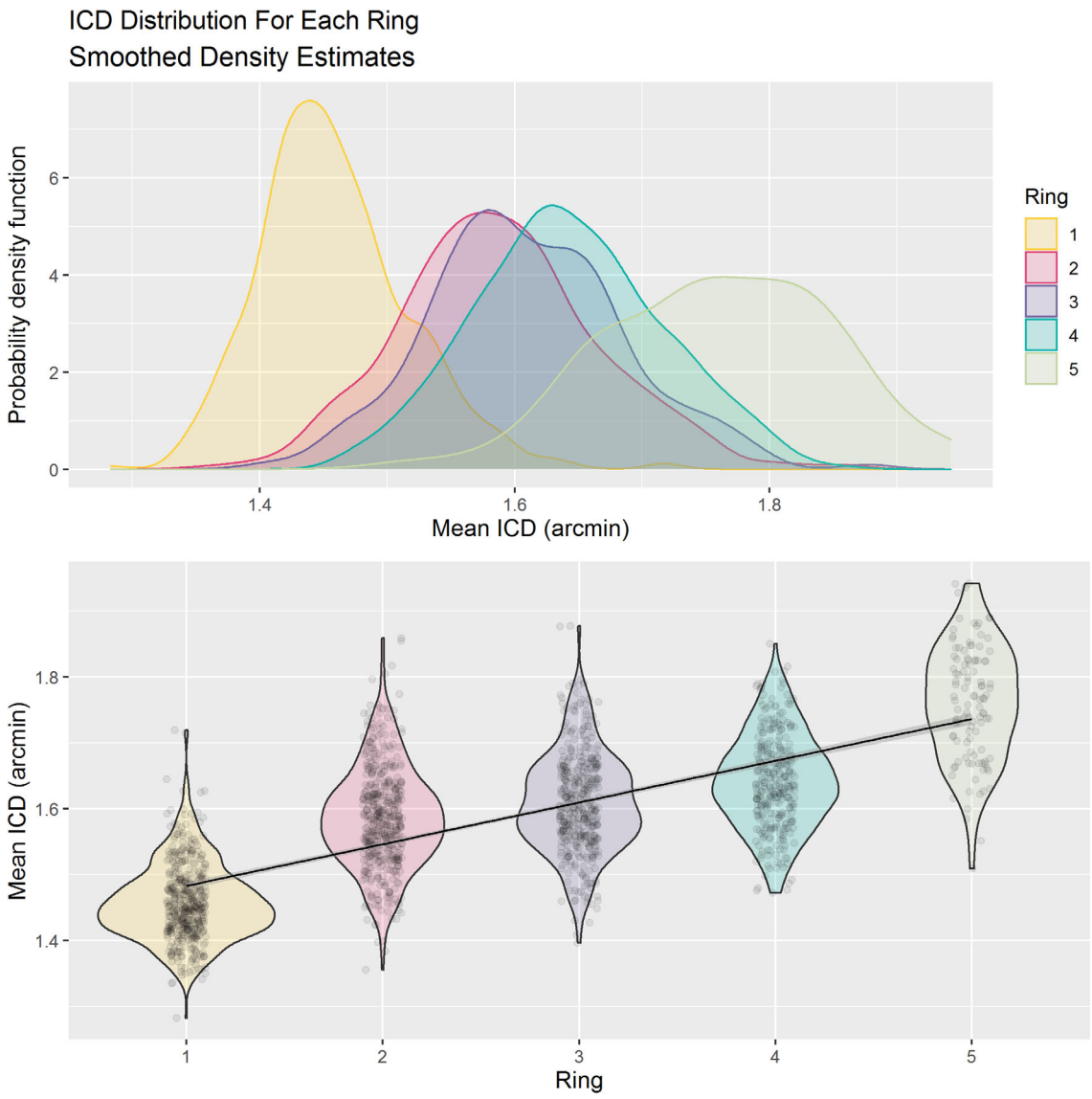

Figure 4. (*Top*) Five overlapping kernel density estimates (smoothed histogram) illustrate the shape of mean angular ICD (arcmin) distribution in five groups of retinal loci from Grids A (ring numbers 1 and 2) and B (ring numbers 2, 3, and 4). (*Bottom*) A violin plot showing the trend for the mean angular ICD to increase as the ring number (diameter) increases (β estimate = 0.08 arcmin per ring number, 95% CI; 0.07 to 0.08 arcmin, $P < 0.01$). Ring 1 (2°), ring 2 (3°), ring 3 (3.2° and 4.2°), ring 4 (5.1° and 5.8°), and ring 5 (7.1° and 7.6°).

sensitivity reduction observed in these studies can be attributed to the use of a Goldmann size III stimulus, which is larger than the critical area within the central 15°, contributing to partial summation in this region.[34] Unlike previous reports, we did not find a significant decrease in DLS with increasing age (β estimate = −0.02 dB/year, 95% CI; −0.06 to 0.01 dB, $P = 0.23$), but this could be due to our small sample size.[35,37–39]

To examine the cellular basis for the DLS gradient across the macular region, we used the AO-FIO device to measure the photoreceptor cell packing arrangement. Reference values of CD provided by Curcio and colleagues'[40] histological study on eight whole retinal flat mounts showed a very sharp decline in CD in the central 1.25° followed by a less rapid decline from 1.25° to 20° whereupon it asymptoted to a plateau region extending from 20° to 60°. In large scale studies using both AO-FIO and adaptive optics scanning laser ophthalmoscopy (AO-SLO) imaging devices, cone density values obtained were comparable to our findings, across a range of eccentricities.[41–43] In addition to CD, AO provides cone separation and regularity metrics that are important

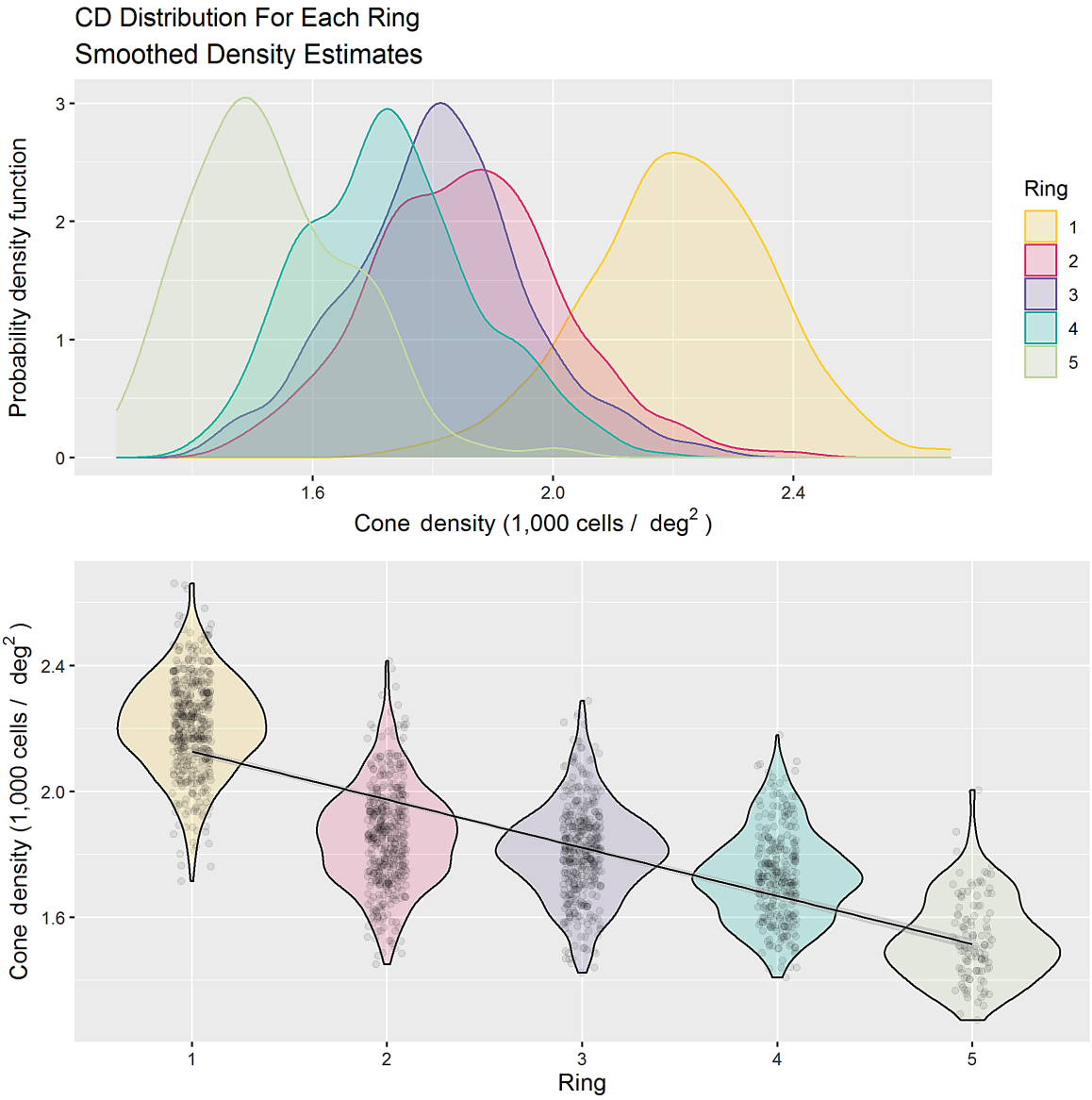

Figure 5. (*Top*) Five overlapping kernel density estimates (smoothed histogram) illustrate the shape of mean angular CD (cells/deg^2) distribution in five groups of retinal loci from Grids A (ring numbers 1 and 2) and B (ring numbers 2, 3, and 4). (*Bottom*) A violin plot showing the trend for the mean angular CD to decrease as the ring number (diameter) increases (β estimate = -0.18×1000 cell/deg^2 per ring number, 95% CI; -0.19 to -0.17×1000 cell/deg^2, $P < 0.01$). Ring 1 (2°), ring 2 (3°), ring 3 (3.2° and 4.2°), ring 4 (5.1° and 5.8°), and ring 5 (7.1° and 7.6°).

parameters of the cone mosaic. We found a significant decrease in CD and an increase in ICD with increasing eccentricity, which is in agreement with previous reports.[14,25,40–42,44–46] The CD and spacing values at each retinal eccentricity are within the reference ranges. It is well recognized that the ability to resolve grating stimulus relates to cone photoreceptor separation in the foveal center. However, MAIA perimetry measures DLS, which is in terms of visual contrast rather than resolution. Therefore it cannot be assumed that there is a similar relationship between DLS and photoreceptor distribution metrics in foveal, parafoveal, and perifoveal regions of the macula.

It is now well accepted that the spacing and receptive field sizes of the midget retinal ganglion cells (mRGCs), rather than cones, contribute to the threshold of visual contrast (DLS) and visual resolution, independent of retinal location.[15,47–50] Hirooka and colleagues[51] found a significant correlation between RGC layer thickness and retinal sensitivity. The 1:1 signal processing from a single cone to a single mRGC in the central fovea may explain the matching visual resolution predicted from Nyquist frequency of cones and mRGCs.[49,52,53] Conversely, eccentricity-dependent decrease in RGC density and increase in its spacing in the human retina[54,55] might contribute to diminished

Table 3. Mixed-Effects Model of Sensitivity Versus Cone Parameters Adjusted for Age and Distance From the Fovea With 95% CI

Cone Distribution Metrics	Grid A β Estimate (95% CI)	Grid B β Estimate (95% CI)	Grid C β Estimate (95% CI)
Angular CD [1000 cells/deg^2]	0.25 (−0.50, 1.00)	−0.05 (−0.86, 0.77)	0.85* (0.10, 1.61)
Area CD [1000 cells/mm^2]	0.03 (−0.03, 0.09)	0.00 (−0.07, 0.07)	0.06* (0.00, 0.13)
Mean angular FND [arcmin]	−0.41 (−1.27, 0.44)	−0.23 (−1.01, 0.55)	−0.74 (−1.62, 0.15)
Mean linear FND [µm]	−0.10 (−0.28, 0.07)	−0.05 (−0.21, 0.11)	−0.14 (−0.33, 0.04)
Mean angular ICD [arcmin]	−0.74 (−2.42, 0.95)	−0.06 (−1.56, 1.44)	−1.36 (−2.93, 0.20)
Mean linear ICD [µm]	−0.19 (−0.54, 0.15)	−0.03 (−0.33, 0.28)	−0.26 (−0.58, 0.06)
Mean angular NND [arcmin]	−0.17 (−1.74, 1.39)	0.36 (−1.00, 1.71)	−0.11 (−1.51, 1.29)
Mean linear NND [µm]	−0.06 (−0.38, 0.26)	0.06 (−0.21, 0.34)	−0.01 (−0.30, 0.27)
Mean linear NND from density [µm]	−0.20 (−0.61, 0.22)	0.00 (−0.37, 0.37)	−0.35 (−0.72, 0.02)
NoNR	0.06 (−0.06, 0.19)	−0.01 (−0.13, 0.12)	−0.00 (−0.15, 0.14)
Proportion 6-sided cells [%]	−0.00 (−0.02, 0.01)	−0.00 (−0.02, 0.01)	−0.01 (−0.02, 0.01)
Ratio mean ICD/NND from density	−1.30 (−5.90, 3.30)	−0.58 (−4.65, 3.48)	0.63 (−4.28, 5.54)
Ratio mean NND/NND from density	0.51 (−2.76, 3.78)	0.96 (−2.10, 4.02)	2.73 (−0.80, 6.27)
Regularity ICD	0.07 (−0.03, 0.18)	0.02 (−0.08, 0.12)	−0.01 (−0.13, 0.11)
Regularity NND	0.02 (−0.05, 0.09)	0.05 (−0.03, 0.14)	0.04 (−0.06, 0.14)

FND, farthest neighbor distance; NoNR, number of neighbors regularity.
*Significance $P < 0.05$.

Table 4. Mixed-Effects Model for Cone Density

	β Estimate	95% CI	*P* Value
Grid A			
Intercept	28.00	27.10, 28.90	<0.01
Age [years]	−0.03	−0.07, 0.01	0.12
Retinal eccentricity [deg]	−0.58	−0.91, −0.24	<0.01
Cone density [1000 cell/deg^2]	0.25	−0.50, 1.00	0.51
Grid B			
Intercept	27.92	27.41, 28.44	<0.01
Age [years]	−0.02	−0.06, 0.02	0.30
Retinal eccentricity [deg]	−0.12	−0.22, −0.02	0.02
Cone density [1000 cell/deg^2]	−0.05	−0.86, 0.77	0.91
Grid C			
Intercept	28.42	27.84, 29.00	<0.01
Age [years]	−0.01	−0.05, 0.03	0.69
Retinal eccentricity [deg]	−0.23	−0.35, −0.11	<0.01
Cone density [1000 cell/deg^2]	0.85	0.10, 1.61	0.03

correlation between cone mosaic metrics and DLS. Based on calculations, Kwon and Liu[50] elucidated that, despite nonuniform distribution of the RGCs, approximately 14 RGCs are involved in the process of complete summation for luminance contrast detection across the human retina.

A more recent work examined the relationship between cone photoreceptor spacing and retinal DLS, given macular perimetry is now also used for investigating macular photoreceptor cell dysfunction and loss. Supriya and colleagues[14] reported a significant reduction in both CD and retinal DLS from 2° to 3° in all quadrants in healthy subjects. They found a significant correlation between area CD in the fovea and retinal DLS in all quadrants at both eccentricities. Both CD and retinal DLS were significantly higher at the horizontal meridian compared to the vertical meridian at 2° and 3° locations.[14] We observed

Table 5. Mixed-Effects Model for Mean ICD

	β Estimate	95% CI	*P* Value
Grid A			
Intercept	28.01	27.15, 28.86	<0.01
Age [years]	−0.03	−0.07, 0.01	0.12
Retinal eccentricity [deg]	−0.57	−0.87, −0.27	<0.01
Mean angular ICD [arcmin]	−0.74	−2.42, 0.95	0.39
Grid B			
Intercept	27.93	27.42, 28.44	<0.01
Age [years]	−0.02	−0.06, 0.02	0.30
Retinal eccentricity [deg]	−0.11	−0.21, −0.01	0.03
Mean angular ICD [arcmin]	−0.06	−1.56, 1.44	0.94
Grid C			
Intercept	28.40	27.82, 28.98	<0.01
Age [years]	−0.01	−0.05, 0.03	0.68
Retinal eccentricity [deg]	−0.26	−0.37, −0.15	<0.01
Mean angular ICD [arcmin]	−1.36	−2.93, 0.20	0.09

a significant correlation between cone density and DLS only across Grid C. Although measures based on both angular and areal units reached statistical significance, the correlation was greater for the angular units. Wang and colleagues[56] showed that despite retinal stretching, angular cone density within and outside the fovea increases with increasing axial length in myopic eyes. They concluded that unexplained low best-corrected visual acuity observed in some of the patients with myopia may not be attributed to cone density changes due to retinal stretching.[56] Our results further support the assertion that factors other than cone packing contribute to DLS across the foveal and parafoveal regions.

Although this is the first study to examine the relationship between cone metrics and retinal DLS across the macular region in which precise alignment between the two imaging modalities was achieved, there are several limitations in the study design that should be considered when interpreting our findings. Our overall sample size was small (only 40 eyes) and a large proportion of subjects had poor AO image quality in the perifoveal regions resulting in a low number of images considered suitable for calculating the cone distribution metrics at 7° from the foveal center. We could not measure CD and ICD closer than 2° from the foveal center because of the inherent limitation of AO-FIO in resolving foveal cones. We did not measure the ganglion cell complex thickness, RGC density and spacing, or Ricco's area. Hence, we cannot confirm whether the decrease in DLS at 5° and 7° is driven by RGC receptive field size. In addition, we were unable to measure rod contribution to the measured DLS, as well as rod mosaic characteristics; both inabilities are inherent limitations of the technologies used in this study. Rod contribution to mesopic visual perception is thought to be mediated via rod-cone pathway interactions either through the rod-cone gap junctions or through rod bipolar cells and amacrine cells to cone bipolar cells.[57] Given the close interaction between the rod and cone systems in mesopic vision, previous work has proposed that rod and cone signals generated under mesopic conditions are interchangeable in terms of postreceptoral processing.[58] Therefore cone parameters alone would only contribute to a portion of mesopic retinal DLS, and further studies are needed to examine in parallel rod spatial distribution. Finally, intersession test-retest variability of DLS in normal individuals is greater than the variability seen across retinal loci. Although we found a statistically significant correlation between CD and DLS on Grid C, the clinical importance of the change in DLS and the utility of DLS as a proxy measure of CD is questionable.

The present study shows that the contribution of cone packing to retinal DLS is limited to Grid C, most likely because of the extended testing field and greater sampling density. Investigation of a larger sample size, along with measurement of RGC distribution, may be necessary to confirm the contribution of RGC density/spacing to retinal DLS. AO-SLO–based microperimetry using smaller stimulus sizes may be more useful to study Ricco's area changes at the central macula.[59] Furthermore, measurement of retinal DLS with compensation of higher -degree optical aberrations might clarify the capacity of retinal DLS assessment in the detection of cone and RGC dysfunction in pathology.

Acknowledgments

Supported by Ophthalmic Research Institute of Australia (DMS, FKC); Bayer Global Ophthalmology Awards Program (FKC); National Health and Medical Research Council (APP1142962, FKC); Telethon Perth Children's Hospital Research Fund (DMS, DAC, FKC); McCusker Charitable Foundation; University of Western Australia Postgraduate Award (DR).

Disclosure: **D.M. Sampson,** None; **D. Roshandel,** None; **A.L. Chew,** None; **Y. Wang,** None; **P.G. Stevenson,** None; **M.N. Cooper,** None; **E. Ong,** None; **L. Wong,** None; **J. La,** None; **D. Alonso-Caneiro,** None; **E. Chelva,** None; **J.C. Khan,** None; **D.D. Sampson,** None; **F.K. Chen,** None

[*] DMS and DR contributed equally to this work.

References

1. Pollak H, Wilson D. Absolute and differential light sensitivity of the dark-adapting eye. *Nature.* 1945;156:299–300.
2. Flammer J, Drance SM, Zulauf M. Differential light threshold. Short- and long-term fluctuation in patients with glaucoma, normal controls, and patients with suspected glaucoma. *Arch Ophthalmol.* 1984;102:704–706.
3. Wildberger H. Neuropathies of the optic nerve and visual evoked potentials with special reference to color vision and differential light threshold measured with the computer perimeter OCTOPUS. *Doc Ophthalmol.* 1984;58:147–227.
4. Chauhan BC, Drance SM, Douglas GR. The effect of long-term intraocular pressure reduction on the differential light sensitivity in glaucoma suspects. *Invest Ophthalmol Vis Sci.* 1988;29:1478–1485.
5. Heijl A. Lack of diffuse loss of differential light sensitivity in early glaucoma. *Acta Ophthalmol.* 1989;67:353–360.
6. Bek T. Localized retinal morphology and differential light sensitivity in diabetic retinopathy. Methodology and clinical results. *Acta Ophthalmol Suppl.* 1992;207:1–36.
7. Susanna BN, Ogata NG, Daga FB, Susanna CN, Diniz-Filho A, Medeiros FA. Association between rates of visual field progression and intraocular pressure measurements obtained by different tonometers. *Ophthalmology.* 2019;126:49–54.
8. Jolly JK, Xue K, Edwards TL, Groppe M, MacLaren RE. Characterizing the natural history of visual function in choroideremia using microperimetry and multimodal retinal imaging. *Invest Ophthalmol Vis Sci.* 2017;58:5575–5583.
9. Chew EY, Clemons TE, Jaffe GJ, et al. Effect of ciliary neurotrophic factor on retinal neurodegeneration in patients with macular telangiectasia type 2: A randomized clinical trial. *Ophthalmology.* 2019;126:540–549.
10. Cassels NK, Wild JM, Margrain TH, Chong V, Acton JH. The use of microperimetry in assessing visual function in age-related macular degeneration. *Surv Ophthalmol.* 2018;63:40–55.
11. Jacobs NA, Patterson IH. Variability of the hill of vision and its significance in automated perimetry. *Br J Ophthalmol.* 1985;69:824–826.
12. Hermann A, Paetzold J, Vonthein R, Krapp E, Rauscher S, Schiefer U. Age-dependent normative values for differential luminance sensitivity in automated static perimetry using the Octopus 101. *Acta Ophthalmol.* 2008;86:446–455.
13. Astle AT, Ali I, Denniss J. Central visual field sensitivity data from microperimetry with spatially dense sampling. *Data Brief.* 2016;9:673–675.
14. Supriya D, Shwetha M, Anupama KK, et al. Structural and function correlation of cone packing utilizing adaptive optics and microperimetry. *Biomed Res Int.* 2015;2015:968672.
15. Garway-Heath DF, Caprioli J, Fitzke FW, Hitchings RA. Scaling the hill of vision: the physiological relationship between light sensitivity and ganglion cell numbers. *Invest Ophthalmol Vis Sci.* 2000;41:1774–1782.
16. Bukowska DM, Chew AL, Huynh E, et al. Semi-automated identification of cones in the human retina using circle Hough transform. *Biomed Opt Exp.* 2015;6:4676–4693.
17. Muthiah MN, Gias C, Chen FK, et al. Cone photoreceptor definition on adaptive optics retinal imaging. *Br J Ophthalmol.* 2014;98:1073–1079.
18. Bennett AG, Rudnicka AR, Edgar DF. Improvements on Littmann's method of determining the size of retinal features by fundus photography. *Graefes Arch Clin Exp Ophthalmol.* 1994;232:361–367.
19. Chew AL, Sampson DM, Kashani I, Chen FK. Agreement in cone density derived from gaze-directed single images versus wide-field montage using adaptive optics flood illumination ophthalmoscopy. *Transl Vis Sci Technol.* 2017;6:9.
20. Cooper RF, Wilk MA, Dubra A, Carroll J. Evaluating descriptive metrics of the human photoreceptor mosaic. *Invest Ophthalmol Vis Sci.* 2016;57:2992–3001.

21. Chiu SJ, Lokhnygina Y, Dubis AM, et al. Automatic cone photoreceptor segmentation using graph theory and dynamic programming. *Biomed Opt Exp.* 2013;4:924–937.
22. Garrioch R, Langlo C, Dubis AM, Cooper RF, Dubra A, Carroll J. Repeatability of in vivo parafoveal cone density and spacing measurements. *Optom Vis Sci.* 2012;89:632–643.
23. Song HX, Chui TYP, Zhong ZY, Elsner AE, Burns SA. Variation of cone photoreceptor packing density with retinal eccentricity and age. *Invest Ophthalmol Vis Sci.* 2011;52:7376–7384.
24. Lombardo M, Lombardo G, Schiano Lomoriello D, Ducoli P, Stirpe M, Serrao S. Interocular symmetry of parafoveal photoreceptor cone density distribution. *Retina.* 2013;33:1640–1649.
25. Lombardo M, Serrao S, Ducoli P, Lombardo G. Eccentricity dependent changes of density, spacing and packing arrangement of parafoveal cones. *Ophthalmic Physiol Opt.* 2013;33:516–526.
26. Duncan JL, Zhang YH, Gandhi J, et al. High-resolution imaging with adaptive optics in patients with inherited retinal degeneration. *Invest Ophthalmol Vis Sci.* 2007;48:3283–3291.
27. Roorda A, Williams DR. Optical fiber properties of individual human cones. *J Vis.* 2002;2:404–412.
28. Syed R, Sundquist SM, Ratnam K, et al. High-resolution images of retinal structure in patients with choroideremia. *Invest Ohthalmol Vis Sci.* 2013;54:950–961.
29. Baraas RC, Carroll J, Gunther KL, et al. Adaptive optics retinal imaging reveals S-cone dystrophy in tritan color-vision deficiency. *J Opt Soc Am A Optics Image Sc Vis.* 2007;24:1438–1447.
30. Carroll J, Rossi EA, Porter J, et al. Deletion of the X-linked opsin gene array locus control region (LCR) results in disruption of the cone mosaic. *Vision Res.* 2010;50:1989–1999.
31. Dees EW, Dubra A, Baraas RC. Variability in parafoveal cone mosaic in normal trichromatic individuals. *Biomed Opt Exp.* 2011;2:1351–1358.
32. Morgan JIW, Dubra A, Wolfe R, Merigan WH, Williams DR. In vivo autofluorescence imaging of the human and macaque retinal pigment epithelial cell mosaic. *Invest Ophthalmol Vis Sci.* 2009;50:1350–1359.
33. Galli-Resta L, Novelli E, Kryger Z, Jacobs GH, Reese BE. Modelling the mosaic organization of rod and cone photoreceptors with a minimal-spacing rule. *Eu J Neurosci.* 1999;11:1461–1469.
34. Khuu SK, Kalloniatis M. Spatial summation across the central visual field: implications for visual field testing. *J Vis.* 2015;15:15.11.16.
35. Fujiwara A, Shiragami C, Manabe S, Izumibata S, Murata A, Shiraga F. [Normal values of retinal sensitivity determined by macular integrity assessment]. *Nippon Ganka Gakkai Zasshi.* 2014;118:15–21.
36. Jones PR, Yasoubi N, Nardini M, Rubin GS. Feasibility of macular integrity assessment (MAIA) microperimetry in children: sensitivity, reliability, and fixation stability in healthy observers. *Invest Ophthalmol Vis Sci.* 2016;57:6349–6359.
37. Choi AY, Nivison-Smith L, Khuu SK, Kalloniatis M. Determining spatial summation and its effect on contrast sensitivity across the central 20 degrees of visual field. *PLoS One.* 2016;11:e0158263.
38. Shah VA, Chalam KV. Values for macular perimetry using the MP-1 microperimeter in normal subjects. *Ophthalmic Res.* 2009;41:9–13.
39. Rohrschneider K, Becker M, Schumacher N, Fendrich T, Volcker HE. Normal values for fundus perimetry with the scanning laser ophthalmoscope. *Am J Ophthalmol.* 1998;126:52–58.
40. Curcio CA, Sloan KR, Kalina RE, Hendrickson AE. Human photoreceptor topography. *J Comp Neurol.* 1990;292:497–523.
41. Legras R, Gaudric A, Woog K. Distribution of cone density, spacing and arrangement in adult healthy retinas with adaptive optics flood illumination. *PLoS One.* 2018;13:e0191141.
42. Park SP, Chung JK, Greenstein V, Tsang SH, Chang S. A study of factors affecting the human cone photoreceptor density measured by adaptive optics scanning laser ophthalmoscope. *Exp Eye Res.* 2013;108:1–9.
43. Woog K, Legras R. Distribution of mid-peripheral cones in emmetropic and myopic subjects using adaptive optics flood illumination camera. *Ophthalmic Physiol Opt.* 2019;39:94–103.
44. Feng S, Gale MJ, Fay JD, et al. Assessment of different sampling methods for measuring and representing macular cone density using flood-illuminated adaptive optics. *Invest Ophthalmol Vis Sci.* 2015;56:5751–5763.
45. Wells-Gray EM, Choi SS, Bries A, Doble N. Variation in rod and cone density from the fovea to the mid-periphery in healthy human retinas using adaptive optics scanning laser ophthalmoscopy. *Eye.* 2016;30:1135–1143.
46. Jacob J, Paques M, Krivosic V, et al. Comparing parafoveal cone photoreceptor mosaic metrics in younger and older age groups using an adaptive optics retinal camera. *Ophthalmic Surg Lasers Imaging Retina.* 2017;48:45–50.
47. Glezer VD. The receptive fields of the retina. *Vis Res.* 1965;5:497–525.

48. Rossi EA, Roorda A. The relationship between visual resolution and cone spacing in the human fovea. *Nature Neurosci.* 2010;13:156–157.
49. Woog K, Legras R. Visual resolution and cone spacing in the nasal and inferior retina. *Ophthalmic Physiol Opt.* 2018;38:66–75.
50. Kwon M, Liu R. Linkage between retinal ganglion cell density and the nonuniform spatial integration across the visual field. *Proc Natl Acad Sci USA*. 2019;116:3827–3836.
51. Hirooka K, Misaki K, Nitta E, Ukegawa K, Sato S, Tsujikawa A. Comparison of macular integrity assessment (MAIA), MP-3, and the Humphrey field analyzer in the evaluation of the relationship between the structure and function of the macula. *PLoS One.* 2016;11:e0151000.
52. Sjostrand J, Olsson V, Popovic Z, Conradi N. Quantitative estimations of foveal and extra-foveal retinal circuitry in humans. *Vis Res.* 1999;39:2987–2998.
53. Watson AB. A formula for human retinal ganglion cell receptive field density as a function of visual field location. *J Vis.* 2014;14:15.
54. Curcio CA, Allen KA. Topography of ganglion cells in human retina. *J Comp Neurol.* 1990;300:5–25.
55. Dacey DM. The mosaic of midget ganglion cells in the human retina. *J Neurosci.* 1993;13:5334–5355.
56. Wang Y, Bensaid N, Tiruveedhula P, Ma J, Ravikumar S, Roorda A. Human foveal cone photoreceptor topography and its dependence on eye length. *Elife.* 2019;8:e47148.
57. Cao D, Pokorny J, Smith VC, Zele AJ. Rod contributions to color perception: linear with rod contrast. *Vision Res.* 2008;48:2586–2592.
58. Zele AJ, Kremers J, Feigl B. Mesopic rod and S-cone interactions revealed by modulation thresholds. *J Opt Soc Am A Opt Image Sci Vis.* 2012;29:A19–A26.
59. Tuten WS, Tiruveedhula P, Roorda A. Adaptive optics scanning laser ophthalmoscope-based microperimetry. *Optom Vis Sci.* 2012;89:563–574.